Multi-machine SOLPS-ITER comparison of impurity seeded H-mode radiative divertor regimes with metal walls

V. Rozhansky[1*], E. Kaveeva[1], I. Senichenkov[1], I. Veselova[1], S. Voskoboynikov[1], R.A. Pitts[2], D. Coster[3] , C. Giroud[4], S.Wiesen[5]

[1]*Peter the Great St.Petersburg Polytechnic University, Polytechnicheskaya 29, 195251 St.Petersburg, Russia;*

[2]*ITER Organization, Route de Vinon-sur-Verdon, CS 90 046, 13067 St Paul Lez Durance Cedex, France;*

[3] *Max-Planck Institute for Plasma Physics, D-85748 Garching, Germany;*

[4] *CCFE, Culham Science Centre, Abingdon, OX14 3DB, UK ;*

[5] *Forschungszentrum Jülich GmbH, Institut für Energie- und Klimaforschung - Plasmaphysik, D-52425 Jülich, Germany*

* Corresponding author E-mail: rozhansky@mail.ru

Abstract

SOLPS-ITER modelling databases of three tokamaks - ASDEX-Upgrade, JET and ITER with fluid drifts activated are compared to understand the dependence of edge plasma performance on machine size and other global parameters. Two medium Z extrinsic radiating impurity species (Ne and N) are considered. It is demonstrated that N is better kept in the divertor region than Ne in semi-detached and detached divertor conditions due to smaller first ionization potential (FIP effect). Together with the fact that Ne radiates more efficiently at higher plasma temperatures, this leads to an increase in the efficiency of Ne for divertor heat load control with increasing machine size. In larger machines such as JET and ITER Ne can be as efficient a radiator as N while for ASDEX-Upgrade Ne easily leads to radiation from the pedestal and loss of H-mode stability. The relative roles of various physical effects are compared for the three tokamaks based on both whole databases and in more details for chosen semi-detached regimes with comparable fraction of radiated power. It is shown that for smaller machines drift effects are more significant and divertor asymmetries more pronounced.

Keywords: SOLPS-ITER; divertor regimes; ITER; ASDEX-Upgrade; JET

1. Introduction

During burning plasma operation on ITER, extrinsic impurity seeding will be mandatory for heat flux control at the tungsten (W) divertor vertical targets [1]. A very extensive database of SOLPS plasma boundary code simulations has been compiled for ITER [1], including the most recent advances, obtained with the SOLPS-ITER version, in which for the first time, fluid drifts have been included [2]. These simulations predict that partially detached divertor solutions with acceptable target heat loads will be possible at high divertor neutral pressure on ITER for baseline burning plasmas (Q_{DT} =10, power into the scrape-off layer P_{SOL} = 100 MW), with both neon (Ne) and nitrogen (N) low Z seeded impurity. The divertor compression of both impurities is sufficient to maintain the majority of the radiated power in the target vicinity, and sustain moderate main chamber separatrix impurity concentration (Z_{eff}<2). This is in contrast to both observations [3] and modeling [4] on smaller devices with W divertors, such as ASDEX-Upgrade (AUG), in which Ne compression is reduced in comparison with N and H-mode plasma performance is compromised. However, Ne is preferred on ITER in DT plasmas to avoid impact on machine duty cycle due to the formation of tritiated ammonia [1]. It is thus critical that the fundamental controlling physics responsible for this behavior be understood, in particular the impact of scale size as well as other parameters. This contribution identifies the key factors through a unique SOLPS-ITER simulation study in which Ne-seeded H-mode conditions are compared in the three W divertor devices ASDEX-Upgrade (R=1.65 m), JET (R = 3.0 m) and ITER (R = 6.2 m), spanning a factor of more than 3 in linear dimension in almost equal size intervals. The divertor target configuration (e.g. vertical versus horizontal) plays a significant role in the working regime and asymmetry in both large and moderate size machines [5,6,7]. To distinguish the size and drift effects from other geometrical factors, all three modeled devices are compared in vertical target single null divertor configuration with the ion ∇B drift directed towards the X-point.

For AUG and JET, the modelling input parameters are inspired by existing experimental results, but do not attempt to match a particular discharge. Instead, the full run databases comprising results obtained in previous numerical studies (AUG [4,8] and JET [9,10]) over the past 4 years are presented and analyzed in this paper. Cross-field heat transport coefficients are chosen to match the typical SOL inter-ELM, heat flux widths, λ_q observed on these devices. Under typical H-mode conditions, the separatrix power flows in the two machines are comparable to those at the divertor entrance in the modelled ITER burning plasma. All simulations include fluid drifts and currents, with neutrals traced by the EIRENE code.

Attached, semi-detached and detached divertor conditions are established in all cases by varying Ne or N seeding and deuterium fuel throughput. For detailed analysis a specific pair of runs with N and Ne seeding is chosen for each tokamak. In these specific cases the fraction of input power radiated in the modeling domain is 50%, the separatrix averaged seeded impurity concentration (ratio of separatrix surface averaged impurity density summed over all ionization states to the deuterium ion density) is in the range 1-2% and the outer target is in the semi-detached regime, with detached strike point and attached plasma in the far SOL.

1. Modeling parameters

The simulation regions are presented in Fig.1, showing the EIRENE triangle mesh domain and the narrower, quadrangular fluid plasma modeling domain. On the plasma domain, the EIRENE mesh is adjusted to the plasma mesh with each quadrangle containing two EIRENE cells. Gas puffing is introduced as source of EIRENE neutrals, molecules (for deuterium) or atoms (for all seeded impurities). Including molecular nitrogen and even ammonia formation would be expected to change the simulated pumping rates and recombination patterns [11]. However, molecular radiation is low in comparison to that from atomic ions and molecules play no role in the transport of impurities between the divertor radiation zone and the separatrix (they cannot survive there). Therefore the absence of a molecular impurity description in the simulations should not change the conclusions regarding the efficiencies of the different seed impurities as divertor radiators. The gas puffing locations also differ in the three devices as they are simulated here (see Fig.1). In the case of ITER, typical values of fuel gas puffing (from the top of the main chamber) applied in modeling described here are below 2% of the divertor recycling flux. Shifting the gas puff on ITER to a divertor location (which will be entirely possible on the machine itself) should not be expected to significantly modify the solution. For the fuel gas at least, this has been recently confirmed in a study of ITER divertor performance in low power, pure hydrogen plasmas [12]. Pumping is also introduced on the EIRENE side in the form of surfaces corresponding to pump duct positions with albedo < 1 for all atom/molecule species (see Fig. 1). Figure 2 compares the linear scale sizes of the three tokamaks, showing that the divertor region volume in ITER is comparable to that of the entire plasma volume in AUG. In JET the main plasma volume is of course larger than that of AUG, but the divertor region dimensions are comparable between the two devices. A further important difference between the modeled cases is the safety factor, q_{95}, which is 3 for the JET and ITER simulations, but which is higher (5.5) in the AUG runs.

The modeling for AUG was performed with input power into the core of the simulation domain in the range P_{IN} = 5-15 MW, toroidal magnetic field B_T=2.5T, plasma current I_p= 800 kA, corresponding to typical experimental parameters for high power H-modes. Impurity seeding varied from trace level to that corresponding to almost complete outer target detachment and the formation of a strongly radiation region in the X-point vicinity. The deuterium throughput (2e22 atoms/s) and pumping were kept constant. These runs were considered in [4,8].

The runs for JET were done with B_T=2.7T, I_p= 2.5 MA and with P_{IN} = 16 MW of input power, corresponding to recent high-power experiment with ITER-like triangularity and vertical divertor target geometry [10], with constant deuterium throughput (3.4e22 atoms/s) and varying seeding of Ne and N from trace impurity up to outer target detachment. These modeling results are published in [9,10].

For ITER P_{IN} =100MW, I_p=15 MA, B_T=5.3T, corresponding to the baseline burning plasma scenario at Q_{DT} = 10. Seeding and throughput were varied to keep divertor pressure in the range 5-10 Pa and the separatrix averaged Ne impurity concentration in the range 0.5-2% according to the planned scenarios for ITER divertor operation, which nominally seeks to avoid complete detachment and the formation of an X-point MARFE [1]. The nitrogen concentration was increased up to 15% in a numerical experiment in order to obtain pronounced detachment at the outer target. A selection of these results of ITER modeling were presented in [1,2], but a the full database is published here for the first time. The chosen turbulent transport coefficients (where D, and $\chi_{i,e}$ are the diffusivities for particles and heat) are shown in Fig.3, illustrating the typical approach to describing the H-mode pedestal and near SOL region.

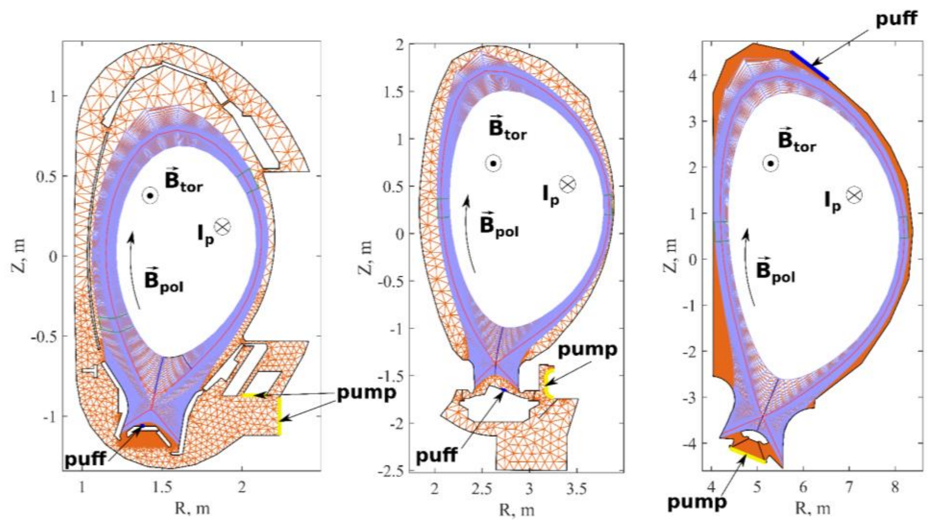

(a) (b) (c)

Fig. 1.Computational domains for (a) AUG, (b) JET and (c) ITER.

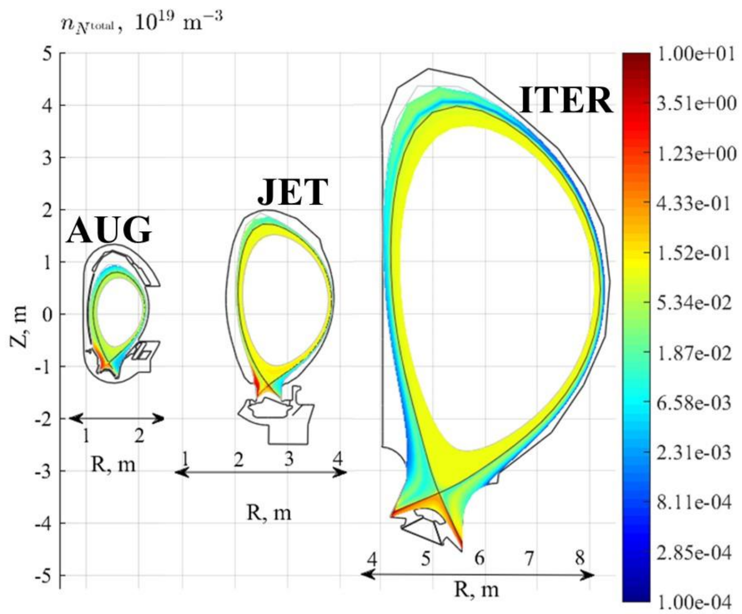

Fig.2. Comparison of dimensions for the 3 tokamaks simulated in this work. Colours correspond to total (neutrals and all ionized states) nitrogen concentrations for runs from Table 1.

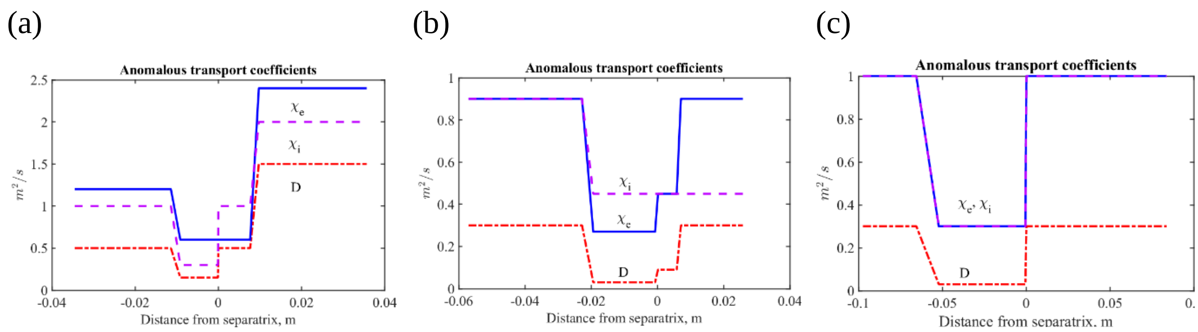

Fig. 3. Transport coefficients at the outer midplane for (a) AUG; (b) JET and (c) ITER.

In addition to analysis of the full databases, three pairs of runs corresponding to the three machines and the two extrinsic seed impurities with approximately the same ratios (~0.5) of radiated power to input power have been isolated to highlight the differences between the three devices (see Table 1). All these cases are in the semi-detached regime, i.e. with a cold outer strike point region (T_e < 5eV) and a hot far SOL. The outer midplane (omp) electron temperature and density profiles for these runs are shown in Fig. 4, and at the outer target in Fig.5, which also contains the target heat flux profile, one of the most important parameters defining acceptable divertor operation on ITER at high performance. For all three machines, there is no significant dependence of both midplane and target profiles of main plasma on the radiating impurity species, while the total radiated power is the same for each machine. The target parameters of the main plasma are determined by the power to the target, with the connection between upstream parameters (pressure and temperatures) and the target being influenced only very slightly by details of the power sink distribution along flux tube. The impurity species can, however, influence the radial distribution of the power sink and therefore the details of target profile shapes. Nevertheless, for a vertical target configuration two distinct zones typically exist: the detached zone with almost all the energy entering the flux tube being dissipated and an attached zone with small power losses along the tube [5]. The radiated power fraction determines the position of the boundary between these regions. For as long as this behavior is maintained for both radiating species, the target profiles look similar.

Table 1 contains main parameters of runs chosen for detailed comparison. A very important parameter for the modelling comparison included in Table 1 is the SOL width $\lambda_{q(e)}$ for electron heat flow associated with parallel heat conductivity. To obtain this value, which depends sensitively of course on the choice of cross-field transport coefficients, heat flow is taken at the outer divertor entrance, divided by the flux tube cross-section at the target and plotted versus distance from the separatrix at the omp. The areas of the flux tubes at the divertor entrance are not used to calculate the heat flow density due to the significant distortion experienced by the presence of the X-point. Instead, flux tubes on the target are used, providing the estimate of the target heat load in the absence of divertor dissipation. Exponential fits in the near SOL region of these curves provide values of $\lambda_{q(e)}$ at the omp. Only the electron heat flow associated with parallel heat conductivity is considered because full energy flows in the smaller machines, AUG and JET are affected by drifts and are not monotonic at the divertor entrance [9]. Exponential fitting for these flows is not reasonable.

3. Results

Several factors have been identified in this modelling which impact the redistribution of main plasma and impurity ions between the divertors and upstream region. These factors will have a strong impact on the impurity radiation, the onset of partial or full detachment and thus finally on the degree of reduction of power to the divertor plates. The most important are discussed below.

3.1. Distribution of ambient D^+ flows and divertor asymmetry

Analysis of the modeling databases discussed here for the three tokamaks supports the statement first made in [13] based only on four AUG and ITER simulations: the role of drifts gradually decreases with increase in device size and magnetic field. In particular, $\vec{E}\times\vec{B}$ drift driven flows decrease below X-point. These flows impact the redistribution of the main plasma from the outer to inner divertor, enforce the onset of inner target detachment and lead to the formation of a high field side high density (HFSHD) region [14,15]. Fig.6(a) plots the ratio of the net $\vec{E}\times\vec{B}$ particle flux of main ions through the PFR to neutral ionization in the outer divertor and the outer target PFR region as a function of the maximum outer target heat load. Evidently, the $\vec{E}\times\vec{B}$ particle flux through the PFR is significant for AUG in attached cases (corresponding to target load > 4 MW/m^2) and most of the semi-detached cases (target load between 0.5 and 4 MW/m^2). It is less significant for JET semi-detached cases (with target load in range 1.5-10 MW/m^2; attached cases in JET have heat load > 10MW/m^2, outer target detachment starts at < 1.5 MW/m^2) and is even less important for ITER (all the runs described here are in the semi-detached regime, corresponding to ITER divertor operation specifications). The qualitative explanation for this behavior was given in [13], but will be reconsidered here in view of its relevance for the main conclusions of this paper.

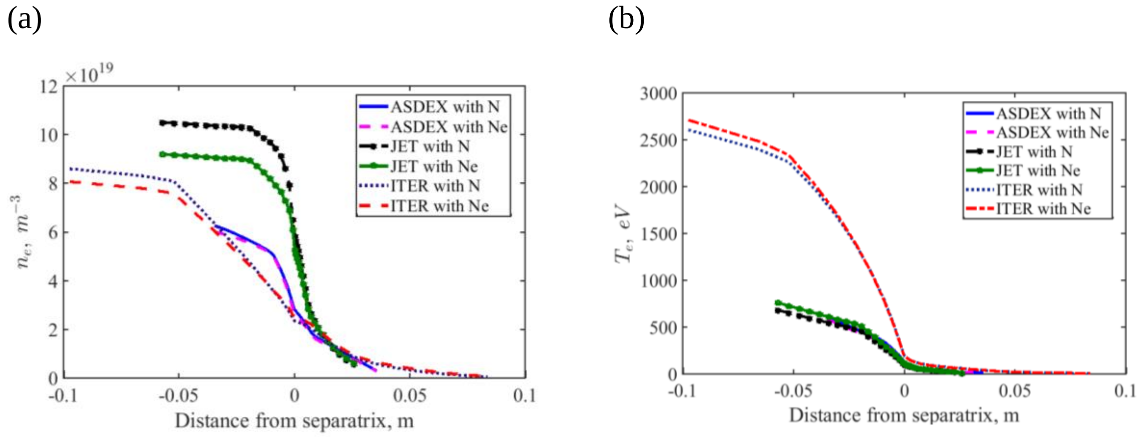

Fig. 4. Outer midplane profiles of (a) electron density and (b) electron temperature for runs from Table 1.

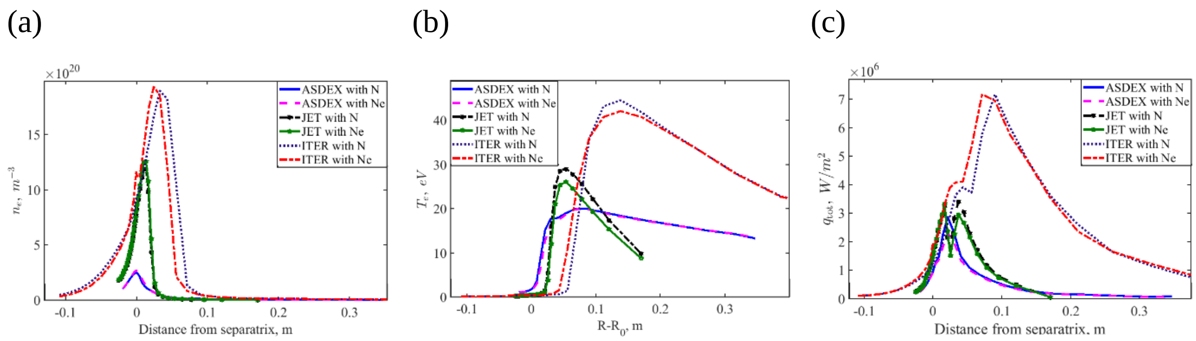

Fig. 5. (a) Electron density, (b) electron temperature and (c) heat load at outer target for runs from Table 1.

Table 1. Key parameters for the specific shot pairs from the three device simulation database chosen for detailed comparisons:

- P_{IN}/R: ratio of power from the core to modeling region (P_{IN}) to major radius.
- B_{tor}, B_{pol}: toroidal magnetic field at magnetic axis and poloidal magnetic field at the omp separatrix.
- $\lambda_{q(e)}$: near SOL width for parallel electron heat flow.
- $q_{(e)\ max}$: maximum value of the electron heat flow associated with parallel heat conductivity; the heat flow is taken at the outer divertor entrance and divided by the flux tube cross-section at the target.
- q_{max}: maximum outer target heat load including plasma, neutral and radiation contributions.
- c_{imp}: concentration of seeded impurity at the main chamber separatrix.

*Note that the radiative losses in the outer divertor include the corresponding part of the private flux region (PFR).

-$P_{rad.,tot}$ total radiation from modeling region

- $T_{e,max}$: maximum electron temperature at the outer divertor entrance.

Tokamak, P_{IN}	ITER, 100 MW		JET, 16 MW		AUG, 5MW	
Radiating impurity	Ne	N	Ne	N	Ne	N
P_{IN}/R (MW/m)	16.1		5.3		3	
B_{tor}, B_{pol} (T)	5.3, 1.23		2.7, 0.52		2.5, 0.34	
$\lambda_{q(e)}$ (mm)	3	3	3	3	1.6	1.4
$q_{(e)\ max}$ outer div. entrance, per target area (MW/m^2)	34	37	19	13	14	19
q_{max} outer target (MW/m^2)	7	7	3.3	3.4	2.3	2.9
c_{imp} , %	1.1	3	1.2	1.2	2.3	1.4
Outer divertor radiation/separatrix power (%)*	26	26	16	15	13	10
$P_{rad.,tot}$, MW	50(50%)	54(54%)	8.6(54%)	8.6(54%)	2.6(52%)	2.4(48%)
$T_{e,max}$ at outer div. entrance (eV)	120	120	67	64	80	77

The drift flux, F_{ExB} of ions along equipotential lines in the PFR towards the inner divertor originates in the ionization zone in the outer SOL close to the separatrix and partially in the PFR. In the case of vertical target configurations, this zone is extended along the separatrix, from the X-point to strike point, where heat flow from upstream meets the neutral flow from the cold region of the PFR. (From the point of view of neutral particle balance, the separatrix is an ideally absorbing surface, so that total ionization in the divertor should be proportional to the neutral pressure in the PFR as long as the semi-detached conditions keep and far SOL plasma is hot. In the database presented here only a few of the runs with the highest seeding in AUG with outer target load < 0.5MW/m^2 and in JET with target load < 1.5MW/m^2 have completely detached plasmas.) The net drift flow of ions through the separatrix between the X-point and the strike point can be estimated as $F_{ExB} = 2\pi R \cdot L_x \cdot n_i \cdot V_{ExB} \approx 2\pi R \cdot n_i \cdot L_x E_{pol} / B$ with L_x the poloidal distance along the separatrix over which the poloidal electric field E_{pol} and poloidal $\vec{E} \times \vec{B}$ velocity V_{ExB} are significant and n_i the ion density. The product $L_x \cdot E_{pol}$ is simply the potential drop in the divertor, from X-point to the target. For the conduction limited or partially detached regimes it can be approximated as $L_x \cdot E_{pol} \approx T_{eX} / e$ with $T_{e,X}$ the electron temperature at the X-point.–The ionization in the divertor can be also estimated through plasma rather than neutral parameters, by assuming it to be, to zero order, approximately equal to the parallel flow of ions towards the divertor plate or the recombination zone. This may be written as $F_{\|} = 2\pi R \cdot L_r \cdot n_i \cdot c_s \cdot \dfrac{B_{pol}}{B}$, where L_r the width of the divertor SOL for particle flow (which can be assumed $\cong \lambda_q$ in semi-detached conditions, when all the flux surfaces carrying the main heat load are in detached or high recycling conditions) and c_s is the ion sound speed. In the outer divertor, the $\vec{E} \times \vec{B}$ to parallel flux density ratio is thus

$$F_{ExB} / F_{\|} = T_{eX} / \left(e c_s B_{pol} L_r \right) \qquad (1)$$

This simple estimate explains the trends in the dependence of “drifts to ionization” ratio on machine parameters (see Fig. 6a). At the same time it should include a numerical factor of smaller than unity, since typically the plasma density in the region with drifts is smaller than that at the plate due to the temperature difference between plate and the region with drifts.

Plasma temperatures at the divertor entrance (X-point level) are higher on ITER than on AUG and JET, though the difference is not dramatic. This latter point can be explained, qualitatively, by the fact that in the semi-detached region of the divertor plasma, T_e is low, of order 1-2 eV so that the temperature drop between divertor and upstream regions is determined to zero order by electron heat conductivity: $T_{e\,X} \sim (L_{\|}q_{\|})^{2/7}$, where $L_{\|}$ is a parallel distance between the cold ionisation front and the upstream location and $q_{\|}$ the parallel heat flux density. The 2/7 power means that the difference between temperatures at the divertor entrance will be not large if the product $L_{\|}q_{\|}$ is at least comparable between the machines.

By far the largest difference between the three devices with regard to the flux ratio in Eq. 1 is the product $B_{pol}L_r$, which is a factor ~8 higher on ITER and factor ~3 on JET than on AUG for the chosen runs (see Table 1). The impact of drifts would thus be expected to be lower on JET than on AUG and still lower on ITER, as observed in the simulations. Fig.6(a) shows that across the whole data set for semi-detached conditions, the drift flow ratio to ionization ratio is indeed 3-4 times larger in AUG than in JET and in JET 3-4 times larger than on ITER, in agreement with the qualitative estimate given above. In both AUG and JET, as the divertor heat loads decrease, the drift flows through the PFR disappear. Such behaviour is also expected from Eq.1, since divertor cooling leads to lower temperature at the divertor entrance.

The estimate Eq.1 does not explicitly contain the machine size; an increase of B_{pol} and λ_q with machine size is not mandatory. However, taking engineering parameters of the existing devices, AUG and JET, and those planned for ITER (all with similar aspect ratio), there is a trend for increasing B_{pol} with machine size. There are also increasing indications that the SOL power width in semi-detached regimes is at least partially determined by turbulence [16,17], so that the typical $\lambda_q \propto 1/B_{pol}$ scaling seen on current devices (including AUG and JET) [18] may be broken at the ITER scale [19,20], leading to a higher λ_q than expected and in fact more consistent with the $\lambda_{q(e)} =$ 3 mm in the ITER simulations described here (Table 1).

The decrease of the relative importance of the PFR drift flow leads to more symmetric divertors for larger machines. The dependence of peak inner target heat load on outer target load is shown in Fig. 6(b). In AUG, redistribution of plasma due to drifts leads to detachment of the inner target so that the inner target heat load is very small for any state of the outer target (for both Ne and N impurity). In JET the redistribution, which increases with hotter outer target, leads to stabilization of the inner target heat load at the level of ~2 MW/m^2 in the simulations, independent of the radiating species. In ITER, the targets are symmetric up to a heat load of 7 MW/m^2. Both in ITER and JET the symmetry of inner and outer divertor heat load increases with decrease of the outer target heat load, i.e. with increase of outer target detachment. This symmetrization is associated with two effects. First, the redistribution of plasma between divertors decreases with cooling of the outer divertor plasma and the corresponding decrease of the poloidal electric field in the divertors (seen for JET and AUG in Fig.6(a)). Second, and more important for ITER, where redistribution of plasma by drifts is modest, a less detached outer target leads to a more asymmetric distribution of impurities, as discussed in the following section, and analyzed in detail for ITER in [2]. When the outer target starts to reattach, impurities concentrate in the inner, more detached divertor, increasing radiation there and therefore increasing the target out-in heat load asymmetry.

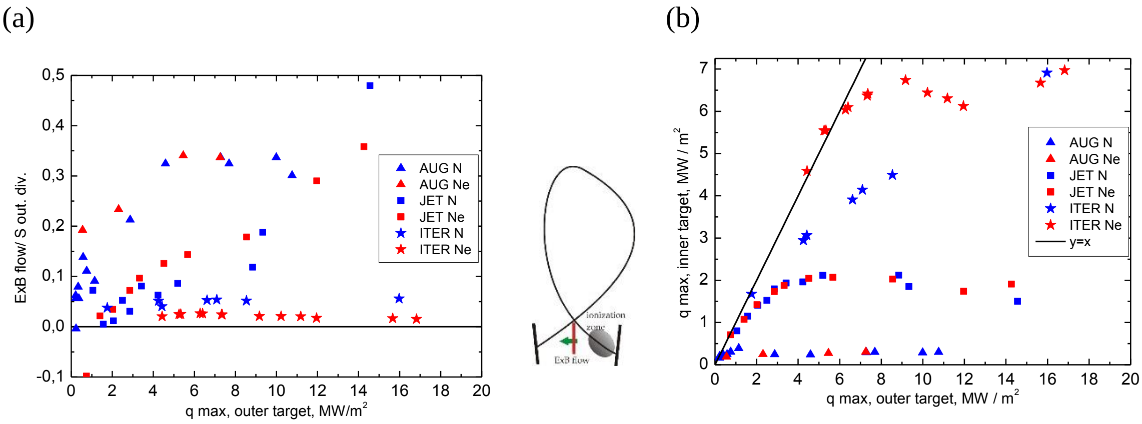

Fig. 6. (a) Ratio of $\vec{E}\times\vec{B}$ driven ion flow below the X-point (through the PFR) to the neutral ionization source in the outer divertor region and (b) peak inner target heat load as functions of peak outer target heat load.

Fig. 7 illustrates the evolution of the 2D electron density distributions with increasing machine size for the three pairs of simulations in Table 1. Regions with high density above 2x10^{20} m^{-3} correspond to low T_e ~ 1-2 eV (see Fig.8). For both Ne and N impurities, these regions are approximately symmetric for ITER, show considerable asymmetry in JET and are completely different at the two divertors in AUG. The cold HFSHD regions arising due to plasma transport by $\vec{E}\times\vec{B}$ drift along the inner divertor, are marked with red ovals [14]. This cold plasma partly comes from the PFR and partly appears in the ionization zone in the vicinity of the inner divertor separatrix. In ITER the extension of the cold region along the inner target due to drift is still visible, with a spatial dimension along the plate of ~20 cm. Although this is comparable to the HFSHD regions in AUG and JET, its physical dimension is negligible in comparison to the ITER divertor size. This area with a similar spatial size for all three machines is also seen in Fig.2 on the nitrogen density profiles. In all three devices the electron density (illustrated by Fig.7) and temperature distribution depend mostly on the total radiation and not on the radiating impurity species, therefore the temperature profiles are shown only for N. This is a feature also seen in Figs.4-5 and discussed above.

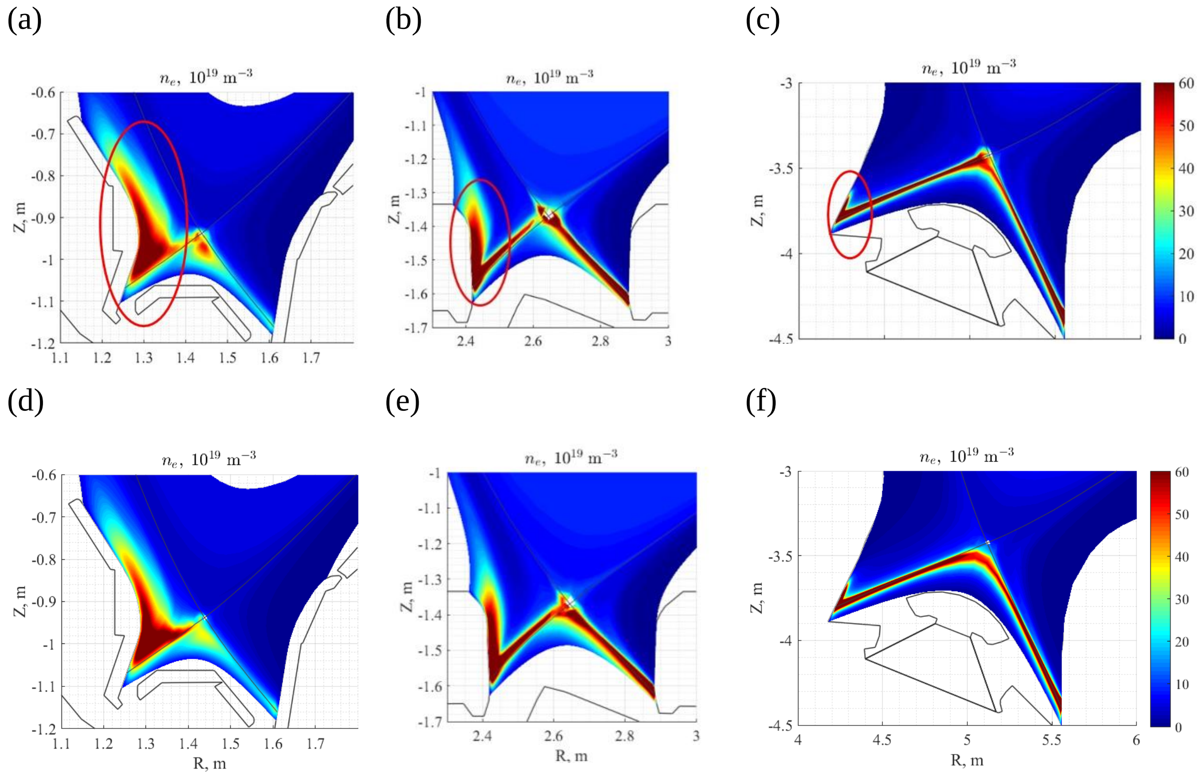

Fig. 7. Electron density for semi-detached runs. (a) AUG with N;(b) JET with N; (c) ITER with N; (d) AUG with Ne; (e) JET with Ne; (f) ITER with Ne.

A further observation is the appearance of a high density region in the PFR with increasing machine size. In AUG high density is seen only in the HFSHD in the inner divertor SOL and is due to $\vec{E}\times\vec{B}$ drag of ions into that region, as discussed above. In the JET simulations, high density bands appear along the separatrix in the PFR and are even more pronounced in ITER than in JET. As a consequence of the larger divertor dimension, the width of the PFR layer along the separatrix (between the X-point and the cold front above the strike point) where the temperature is enough for ionization of deuterium is larger in bigger devices. When the width of this layer becomes comparable to the deuterium ionization length the ionization source in the PFR increases, leading to a density increase. This effect is seen in modeling even without drifts. Analysis of $\vec{E}\times\vec{B}$ flows through separatrix in the outer and inner divertors reveals that in the larger of the three machines (JET and ITER) these flows at the outer divertor side can be higher than at the inner, also leading to plasma accumulation in the PFR. In contrast, in AUG the flow through the inner side of the separatrix dominates. This difference is associated with difference in the mechanism of poloidal electric field formation at divertor separatrix. In AUG the electric field in the cold HFSHD zone arises to support the thermoelectric current [14].

(a) (b) (c)

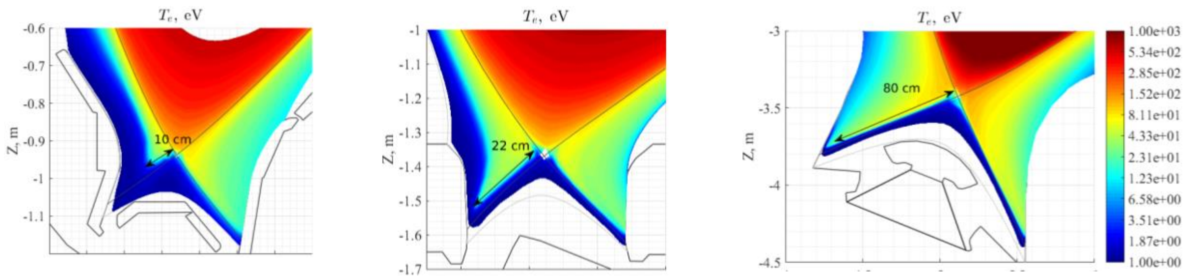

Fig. 8. Electron temperature for semi-detached runs. (a) AUG with N;(b) JET with N; (c) ITER with N. the approximate distance from the ionization front to the X-point is marked in each case.

In ITER and JET, the current associated with charge-exchange friction of ions and neutral atoms gives a significant contribution to current balance in the cold region. The short-circuiting of this current by parallel current gives rise to complex behavior of the electrostatic potential, which will be described in a future publication. Finally, the poloidal electric field in the PFR and at the inner divertor separatrix near the target is directed away from the target, while closer to the X-point it is still directed towards target. As a result, the overall radial flow from the PFR to the inner divertor SOL decreases and plasma accumulates in the PFR. To provide the recycling at the plates in the PFR at the low target temperature in this region a considerable increase of density is necessary, which is seen in the modeling, Fig.7.

Symmetrisation of the divertor plasmas leads to a decrease of flows through the SOL between the divertor plates. In an in-out asymmetric divertor, a neutral flow arises from the inner to outer divertor through the PFR and under divertor structures due to the higher inner divertor neutral pressure. From the modeling it can be concluded that this flow exceeds the plasma flow towards the inner target through PFR. As a result, a plasma flow should exist through the main chamber SOL from the outer to inner divertor. To exclude the Pfirsch Schluter contribution, the symmetric part of the flow between the divertors due to ionization of puffed neutrals in ITER and the recycling flow in the HFSHD region in AUG, the flow from outer to inner divertor can be estimated as the half-sum of the poloidal flows at the outer and inner midplane. The ratio of this flow to the ionization source in both divertors is shown in Fig.9(a) for the three tokamaks. Evidently, this ratio is the lowest for ITER. In moderate sized tokamaks, this flow is considerably modulated by Pfirsch-Schlueter (PS) like flows, compensating ∇B driven flux in the SOL [21]. In larger machines, the relative role of the ∇B drift also decreases in comparison to recycling in the divertor, Fig.9(b), and therefore PS flows do not play a significant role. The ratio of ∇B flow through the upper part of the main chamber separatrix $F_{\nabla B} \approx 2\pi R \cdot 2r \cdot n_{i(u)} \cdot \frac{T_{i(u)}}{eBR}$ to ionization in the divertor can be estimated once again using the assumption (see Eq (1)) that ionization is balanced mainly by parallel flow towards the plate: $F_{\|} = 2\pi R \cdot L_r \cdot n_{i(t)} \cdot c_{s(t)} \cdot \frac{B_{pol}}{B}$. Here subscript (u) denotes upstream and subscript (t) target values of parameters. Using the 2-point model [22], $2n_{i(t)}T_{i(t)} \approx n_{i(u)}T_{i(u)}$ so that:

$$F_{\nabla B} / F_{\|} = q\rho_{ci(t)} / L_r . \tag{2}$$

where q is safety factor. In common with Eq. (1), this ratio decreases with increasing SOL width and magnetic field. It can therefore be concluded that the relative role of drifts in the formation of plasma flows, both in the divertor and in the upstream SOL steadily decreases with increase of machine size and magnetic field for the SOL width chosen in the modelling, Table 1. In the case of the Eich [18] scaling for λ_q the role of the ∇B drift is machine size independent, a fact which is quite natural given its agreement with the Goldston Heuristic Drift model [23]. In the latter, the SOL width is determined by the balance of ∇B drift and parallel flow towards the divertor targets, assumed to be given by $n_{i(u)} \cdot c_{s(u)}$. It should be noted that the Eich scaling was obtained from outer target measurements for H-mode, attached divertor conditions. In most of the simulations discussed here, the outer divertor is in a semi-detached state. The transport coefficients (which determine the upstream λ_q) for the AUG and JET simulations were chosen to reproduce "typical" discharge parameters (but not being matched to any particular experimental pulse). The resulting SOL widths are slightly larger than would be predicted by the scaling.

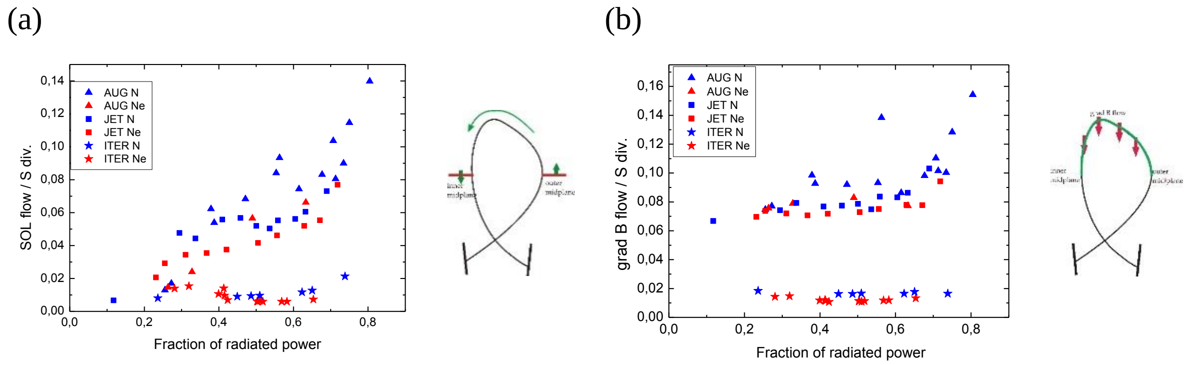

Fig. 9. Ratio of (a) poloidal flow through SOL and (b) radial ∇B flow through the upper main chamber separatrix to ionization in both divertor regions as functions of the ratio of the total radiated power to the power entering computation domain.

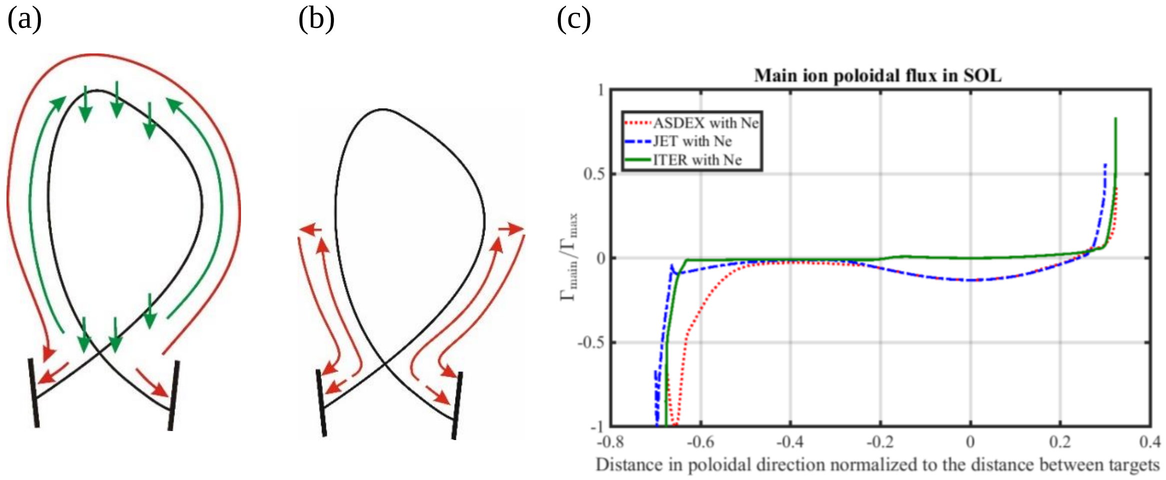

Fig.10. (a) Schematic view of main SOL flows in moderate size machines. PS and ∇B flows are shown in green; flows in the divertor from the ionization front towards plates and net flow from outer to inner divertor in red. (b) As in (a) but for a large device like ITER, where the dominant flows are from the ionization front towards the plates and through the omp. (c) Normalized integral poloidal flows in the SOL for the Ne-seeded simulations in Table 1. Negative flow is from the outer to inner divertor. Zero abscissa corresponds to the omp.

3.2. First ionization potential (FIP) effect

Figure 11 compiles the distributions of normalized impurity density for the simulations in Table 1. Species with higher ionization potential are more effectively extracted from the divertor towards upstream, so that N is retained more efficiently than Ne in the divertor regions in all three modeled machines. This effect was discussed in detail in [4], from which the schematic illustration in Fig. 12 is extracted. In semi-detached and conduction limited regimes in medium to large size devices, the ionization zone of the main fuel is located in the divertor. From this region the ionized fuel particles flow towards the plates. Impurity species with lower ionization potential than that of the fuel are ionized closer to the plates and are dragged by the main ion flow towards the targets. In semi-detached regimes, the parallel temperature gradient in this zone is low so that the thermal force produces only a small deviation of the impurity velocity from that of the main ions. The probability of escape from the divertor for such ions is low and they are retained effectively in the divertor region.

If the impurity ionization potential is higher than that of the fuel atoms, ionization is more probable in the region further upstream. If there are main ion flows towards upstream above the fuel ionization zone, impurity retention in the divertor will be low. Impurity velocities are also more shifted towards the upstream region here due to the higher ion temperature gradient above the ionization front and therefore a larger thermal force, see [4]. As far as this particular effect is concerned, larger devices have no significant advantage over smaller machines since in both cases flows are present above the ionization zone towards upstream locations. In smaller machines, impurities are dragged mostly by PS flows, while for large devices this drag is driven by the flows produced by ionization in the strike point vicinity. The only advantage of large size here is the absence of any pronounced integral flow of main ions from the outer to inner divertor. This flow leads to transport of impurities leaking upstream from the outer to the inner divertor, increasing radiation in the inner divertor and pushing up the divertor asymmetry. Pronounced divertor asymmetry leads to considerable accumulation of impurity in the inner detached divertor before the onset of outer divertor strike point detachment and the transition of the outer target to the semi-detached regime. The stronger divertor asymmetry of smaller machines is thus unfavorable for divertor dissipation of power by impurity seeding.

It is important to note that the FIP effect is most pronounced in semi-detached and detached regimes in which a steep temperature gradient exists with poloidal scale length of several cm, separating cold regions with T_e well below 5 eV and hot plasma with T_e up to ~100 eV. This observation first appeared in the study reported in [9] and is now supported by the analysis of wider database discussed here. In the region closer to the plates where ionization source is small both deuterium and impurity ions are strongly coupled and their poloidal velocity is directed towards the divertor targets. The ionization front for the main ions is situated in narrow zone, part of ions flows towards the plate and other part flows towards upstream. Thermal force here leads to additional impurity velocity directed upstream with respect to that of the main ions. As a consequence, the impurity ionization potential dramatically influences impurity retention, determining the exact position of the impurity ionization front within the steep temperature gradient. This very localized region is also the stagnation point of the main ion and impurity flows.

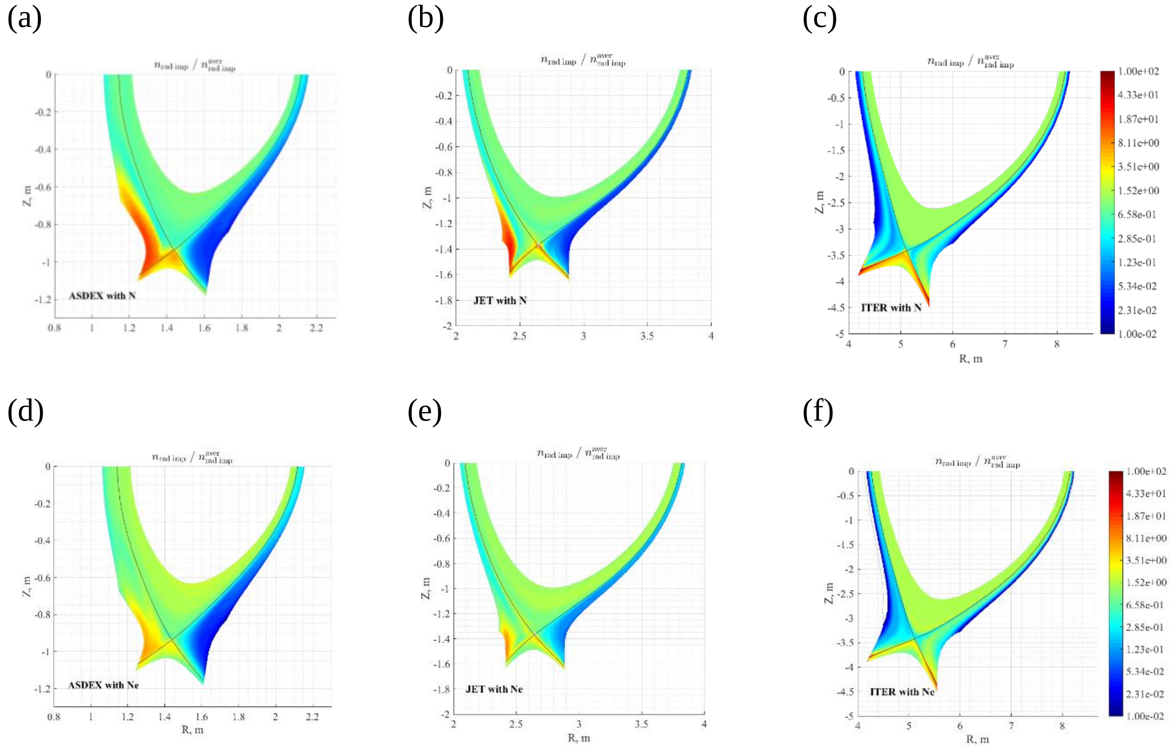

Fig.11. Impurity distribution (normalized to average) for runs from Table 1. (a) AUG with N;(b) JET with N; (c) ITER with N; (d) AUG with Ne; (e) JET with Ne; (f) ITER with Ne.

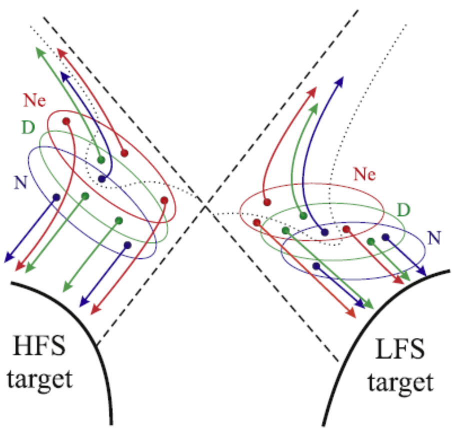

Fig. 12. Illustration of leakage/retention mechanism. Zones of peak ionization are shown schematically by ellipses. Dotted lines represent the stagnation points of poloidal flow. Solid circles show points of ionization and arrows of corresponding color represent the poloidal flow directions. Extracted from [4].

In less detached regimes, the FIP effect is still present but is less pronounced. The ionization rate dependence on temperature is very steep at temperatures lower than the first ionization potential of the atom [22]. When T_e is comparable or higher than the first ionization potentials of all species in the system, the ionization position depends more on the electron density profile than on the temperature distribution. Therefore, for attached conditions when T_e is high almost everywhere in the divertor, the impurity ionization position is less sensitive to the first ionization potential and is less separated spatially for different species of impurities and main ions. In addition, the temperature gradient is less steep in the ionization region and the position of the stagnation point for poloidal impurity flow is determined by several factors, including drifts.

3.3. Position of ionization front

In larger machines the ionization of neutral impurities is shifted closer to the plates and takes place outside the separatrix for both N and Ne, Fig.13. In contrast, in smaller devices the ionization source is located more inside the separatrix, giving rise to a steep density gradient for the main ions, and therefore to inward neoclassical convection for impurities which is determined by the main ion density and temperature gradients [24]. Plots of the radial distribution of main ion and radiating impurity densities are shown in Fig. 4(a) and Fig. 14 respectively.

Fig. 15, demonstrates the role of neoclassical flows and ionization source inside the separatrix in different sized machines with different density and temperature profiles for the specific case of Ne impurity. The sum of the ∇ B and $\vec{E}\times\vec{B}$ drift flows of Ne, representing neoclassical transport in the fluid description of plasma, are compared to those induced by anomalous transport and to the total flow. Anomalous diffusive flow determines the radial density profile. It arises partly to compensate the neoclassical transport and partly to provide the outward transport of particles ionized inside separatrix. In AUG, the total Ne flow arising as a consequence of ionization inside the separatrix provides a significant contribution to the diffusive flow, while in both JET and ITER it is small. In JET, however, the neoclassical transport demands a clearly visible compensating diffusive flow and leads to changes in impurity density profile, seen in Fig.14, while in ITER the Ne density profile is flat. It should be mentioned here that both ion-neutral friction and the thermal force determining neoclassical transport are computed in SOLPS-ITER in the fluid approximation, without kinetic corrections. The neoclassical transport shown here therefore requires further corrections, especially for large machines. Nevertheless, the tendency for a reduction of the neoclassical impact on the impurity density distribution and on heat transport with increase of machine size and magnetic field should persist [25].

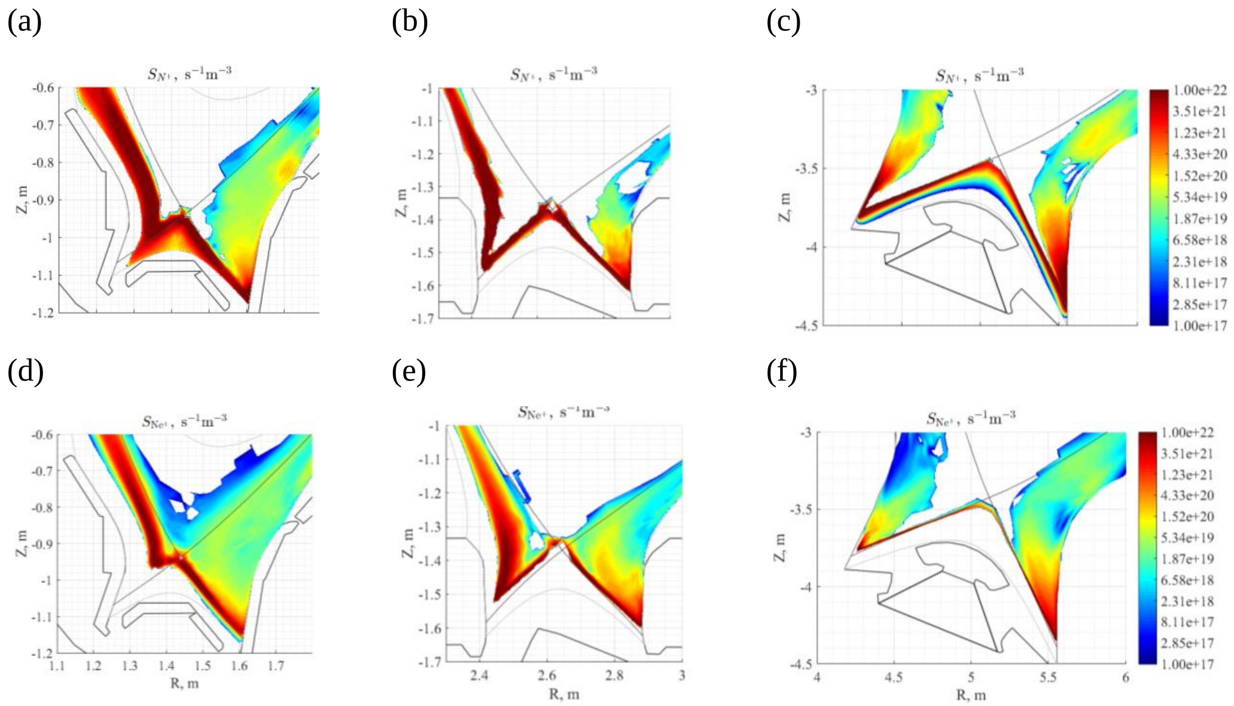

Fig.13. Ionization source of radiating impurity for the simulations in Table 1. (a) AUG with N; (b) JET with N; (c) ITER with N; (d) AUG with Ne; (e) JET with Ne; (f) ITER with Ne.

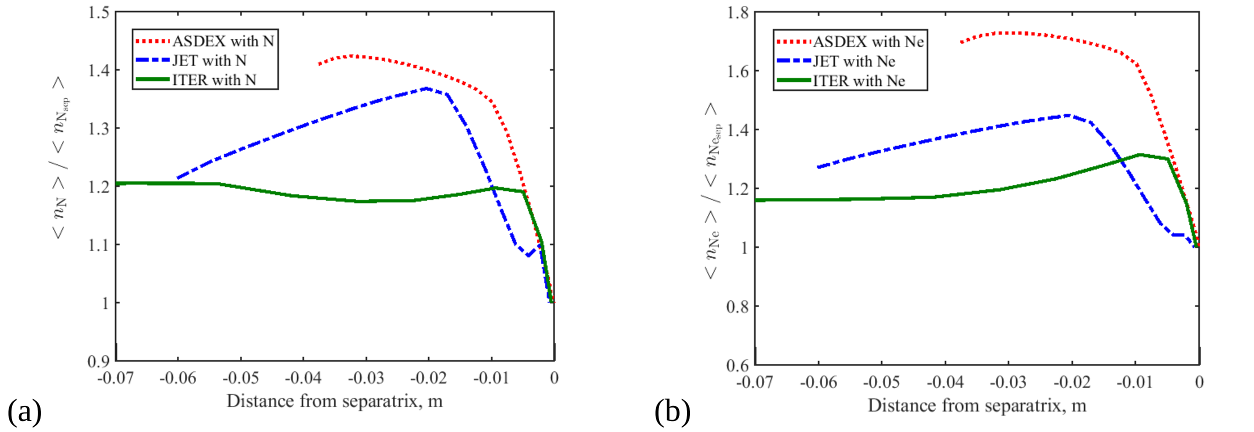

Fig.14. Radial distribution of flux surface averaged impurity density inside the separatrix, normalized to the separatrix value, for the runs from Table 1.

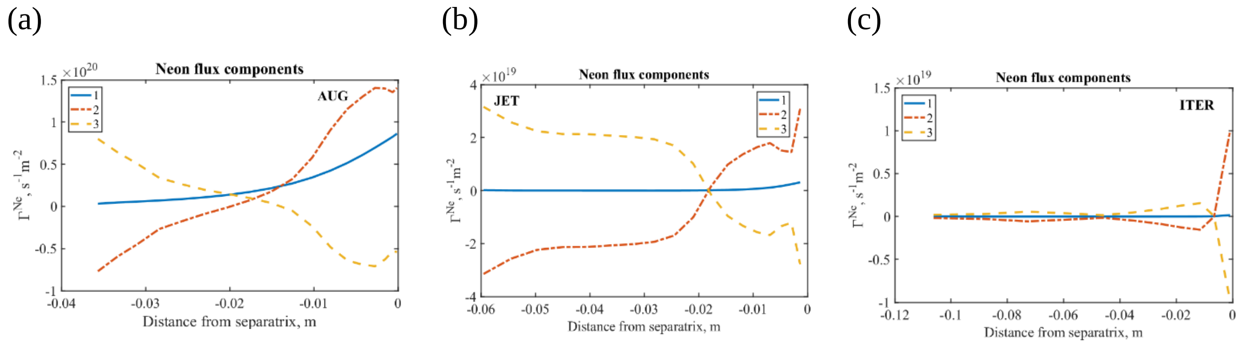

Fig.15. Flux surface averaged Ne ion flow components for the runs from Table 1:
1 – total flow; 2 – diffusive transport; 3 – drift contribution. (a) AUG; (b) JET; (c) ITER.

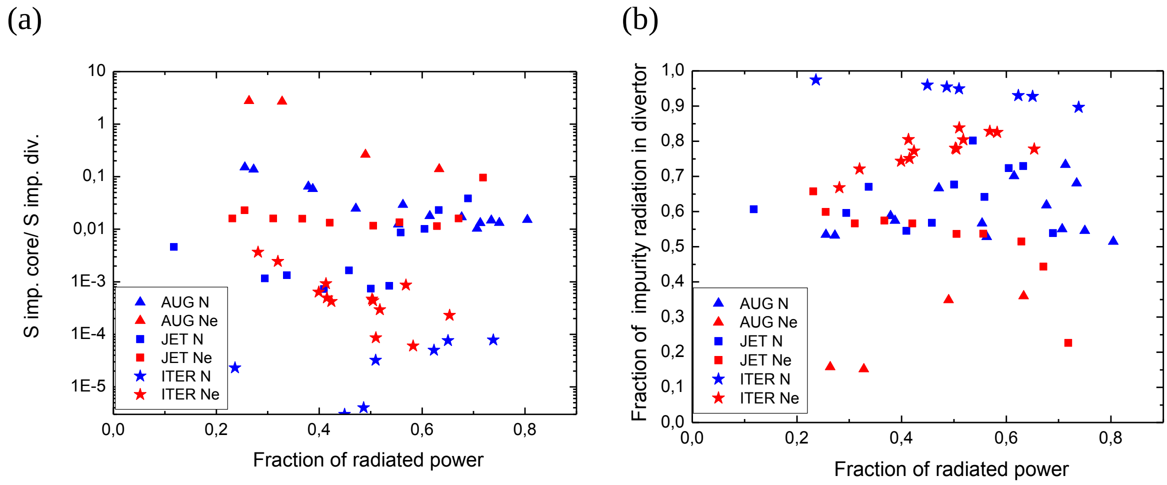

Fig. 16. (a) Ratio of ionization source of impurity (N or Ne), in core region of the computational domain to that in the divertor; (b) ratio of power radiated by impurities in the divertor to the total power radiated by impurity as a function of the fractional radiated power (total radiated power normalized to P_{IN}).

First ionization of impurities inside the separatrix is more probable in smaller machines. Due to its higher ionization potential, neutral Ne reaches the separatrix more easily than N, leading to a higher pedestal ionization source and hence to a higher density inside the separatrix (seen clearly in Fig. 13). In AUG this effect is amplified by divertor asymmetry. The cold front in the inner divertor (Fig. 8(a)) is so close to the X-point that the flow of neutral Ne from the HFSHD region reaches the separatrix and produces an ionization source inside the separatrix comparable to that in the divertor. For AUG, this distance (marked approximately in Fig. 8) is typically 10 cm. Figure 16 gives the ratio of the impurity neutral ionization source inside the separatrix to that in the divertor (below the X-point) for the full simulation dataset. In all three devices it is an order of magnitude higher for Ne than for N and increases with decrease of scale size. In AUG, ionization in the divertor and inside the separatrix are comparable for Ne impurity. Ionized in the H-mode transport barrier region, Ne is dragged towards the top of pedestal by neoclassical convection and finally accumulates in the core.

3.4. Radiation distribution

Since low Z impurity radiation will be the strongest in the region of comparatively low T_e where many partially ionized states exist, impurity radiation in larger machines is more localized in the divertor. This is illustrated in the 2D distributions of radiation per nucleon, shown in Fig.17, where it is also clear that the radiation band for Ne is shifted upstream and is wider than that of N for all three devices. On JET and ITER, this means that even though the strongly radiating region with Ne impurity is more extended than for N seeding at comparable radiated power, both are equally effective for divertor power dissipation. This is illustrated by the distributions of total radiation in Fig.18. The Ne radiation zone is more extended than that of N since Ne has more ionization states and its complete ionization requires higher T_e and more physical space. Even so, in ITER for $P_{rad.,tot}/P_{IN} = 0.5$ the radiation is still localized in the divertor for both Ne and N. In AUG the radiation is shifted towards X-point for both species and while the nitrogen radiation is localized in a narrower band, the Ne radiation inside the separatrix is not negligible as a result of the lower pedestal temperatures. In JET, the situation is intermediate between that in AUG and ITER, at least according to the modelling.

In all three devices there is no impurity radiation in Fig. 18 from the pedestal top region for N, while in AUG with Ne there is a low, but still visible radiation. As mentioned above, this is a consequence of the lower pedestal temperature in AUG (Fig.4b), leading to the persistence of incompletely ionized Ne states (seen also in Fig.17). Neon ions reaching the ITER and JET pedestal top regions are fully stripped due to the high T_e there and cannot radiate, reducing the impact on pedestal power balance. This effect can be amplified by charge-exchange between neutral deuterium and high impurity ionization states. At present, non-resonant charge-exchange is not included in the simulations. In the AUG pedestal region, this effect can increase the population of partially ionized states for Ne with a concomitant increase in their radiation by a factor 5 [26]. On JET this effect is smaller, and for ITER it should be negligible taking into account the orders of magnitude lower neutral deuterium concentration in the pedestal at high performance.

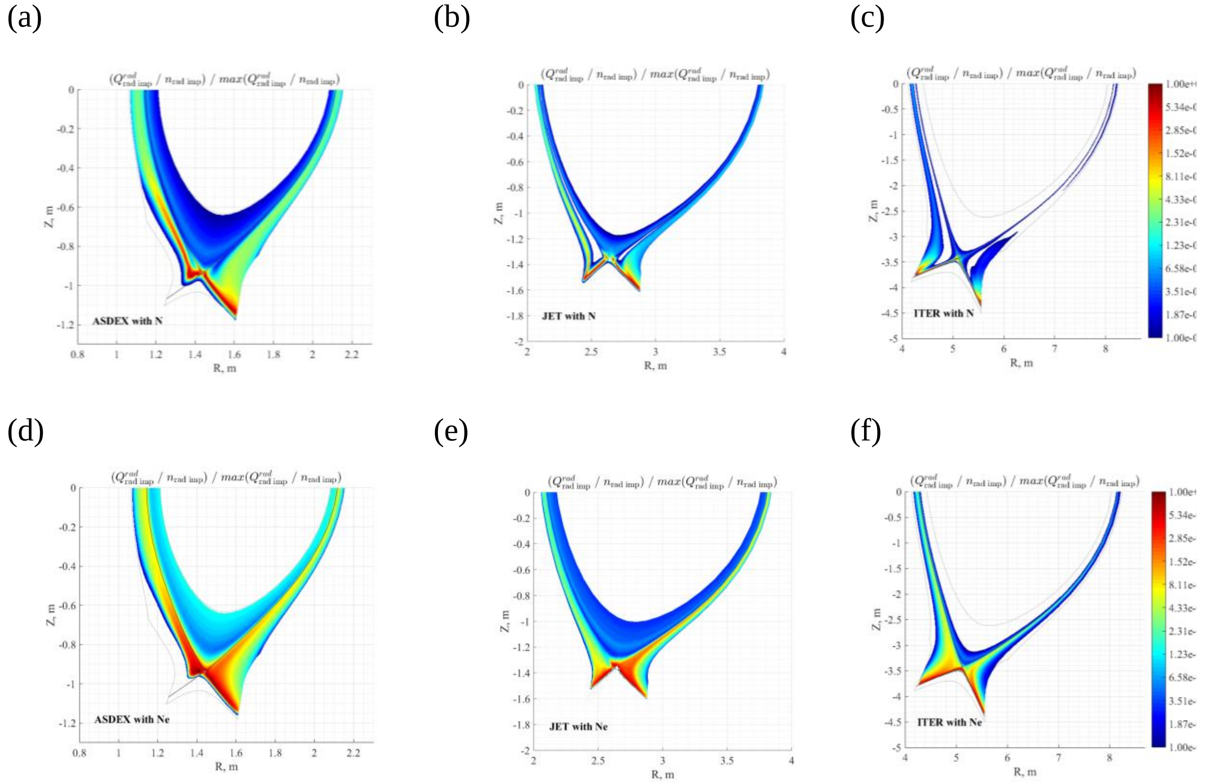

Fig. 17. Impurity radiation per nucleon (normalized to the peak value). (a) N in AUG; (b) N in JET; (c) N in ITER; (d) Ne in AUG; (e) Ne in JET; (f) Ne in ITER.

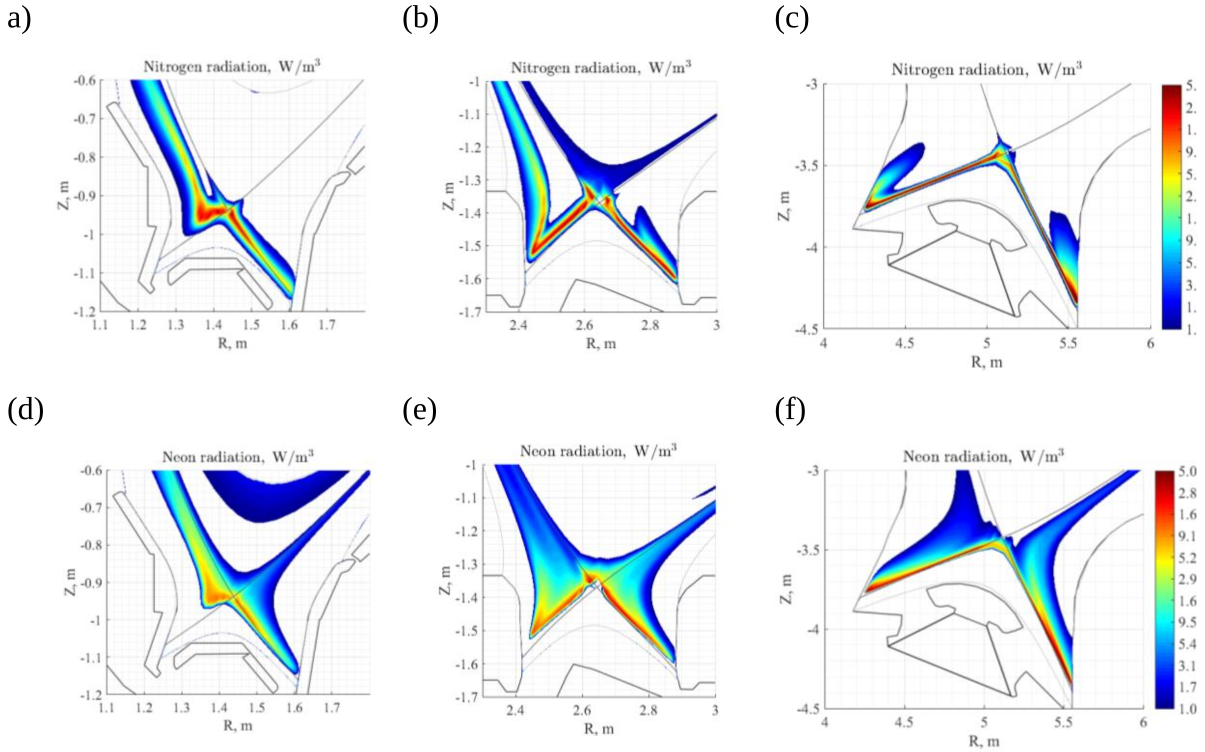

Fig. 18. Impurity radiation distributions for the 3 simulations in Table 1. (a) N in AUG; (b) N in JET; (c) N in ITER; (d) Ne in AUG; (e) Ne in JET; (f) Ne in ITER.

These differences in the distribution of radiation in the three tokamaks and for the two radiating species is further illustrated in Fig. 16(b), which gives the share of impurity radiation in the divertor from the total impurity radiation in the computational domain as a function of the fraction of power radiated by all species (impurities and main ions). As previously noted, for all the machines N radiation is more localized in the divertor than that of Ne and for larger scale size, the divertor localization is higher for both species. In AUG with Ne, the majority of the radiation comes from the region above X-point. This effect would be even more dramatic if the contribution of radiation from the core regions were taken into account. This contribution. not included in the present modeling, would not be negligible on AUG, much smaller on JET and negligible on ITER.

On the basis of very simple considerations, omitting any details of divertor asymmetry, the difference in radiation behavior can be explained as follows. The radiation of given power entering a flux tube requires a certain volume for given plasma density and impurity concentration. If this volume in the divertor is lower than this threshold value, the impurity concentration or plasma density should be increased to obtain a semi-detached solution. If it is larger, a cold detached region arises below the radiative zone. In addition, due to the finite ionization length, there is a lower limit on the width of the radiation zone, increasing with the atomic number of the radiating impurity, even in the high temperature region. From the simulations presented here the ITER divertor volume is sufficient both for efficient radiation of the SOL power under fusion burn conditions and to contain all the partially ionized states of Ne. As a consequence, Ne appears to be an even more acceptable radiator than N in ITER since (see Table 1) the same divertor radiation fraction requires 1% of Ne and 3% of N at the separatrix, corresponding to approximately the same Z_{eff} at omp separatrix ~2 and at the pedestal top ~1.5.

4. CONCLUSIONS

Impurity seeding for divertor power dissipation and control of stationary target heat fluxes will be mandatory on ITER during burning plasma operation. At present, based on experiments on current all-metal devices, of the two main candidate species for ITER, N is found to perform best in terms of divertor localization of the radiation, whilst Ne can be more problematic, leading to unfavourably high radiation in the pedestal region of H-mode plasmas. However, Ne is preferred on ITER due to the absence of chemistry (ammonia formation), which can be problematic from the point of view of the fuel cycle. Plasma boundary studies using the SOLPS suite of codes [1, 13] have found that both Ne and N would be acceptable radiators for ITER. This paper has extended these studies constituting, for the first time, a multi-machine simulation exercise using the SOLPS-ITER code with fluid drifts activated, of N and Ne impurity seeded, high power H-mode scenarios on the three all-metal devices ASDEX Upgrade, JET and ITER. This provides a unique assessment of divertor performance with the two radiators as machine scale size is increased by a factor of 3. The main conclusions of this study can be summarized as follows:

— Outer and inner divertors are more symmetric for larger machines, with the symmetry increasing with higher seeding, i.e. for more detached divertors;
— The ambient plasma main ion and impurity flows from the outer to inner divertor both through the main chamber SOL and the PFR are more significant for smaller devices such as AUG and are less important for larger machines;
— In larger devices ionization of neutral particles takes place closer to the targets and neutral impurities are better confined in the divertor;
— First Ionization Potential effect: impurities with higher ionization potential are more effectively extracted from the divertor towards upstream, so that N is retained better than Ne in the divertor region;
— According to the modelling, which confirms earlier studies for ITER, in larger devices, due to the higher plasma temperature and physical size, Ne radiation is as efficiently localized in the divertor region as for N, so that the two species are entirely comparable for target heat load control in ITER and should also be nearly equally effective in JET.

ACKNOWLEDGEMENTS

This work was supported by Russian Science Foundation, grant no. 20-52-53025 and conducted partially under the auspices of the ITER Scientist Fellow Network. Numerical calculations were performed at the Polytechnic Supercomputer Center at Peter the Great St. Petersburg Polytechnic University. The views and opinions expressed herein do not necessarily reflect those of the ITER Organization. This work has been carried out within the framework of the EUROfusion Consortium and has received funding from the Euratom research and training programme 2014-2018 and 2019-2020 under grant agreement No 633053. The views and opinions expressed herein do not necessarily reflect those of the European Commission.

REFERENCES

[1] Pitts R. A. et al. 2019 *Nucl. Mater. Energy* **20** 100696

[2] Kaveeva E. et al. 2020 *Nucl. Fusion* **60** 046019

[3] Bernert M. et al. 2017 *Nucl. Mater. and Energy* **12** 111

[4] Senichenkov I. et al. 2019 *Plasma Phys. Contr. Fusion* **61** 045013

[5] Loarte A. 2001 *Plasma Phys. Control. Fusion* **43** R183–R224

[6] Pitts, R. A., et al, Status and physics basis of the ITER divertor Physica Scripta, IOP Publishing, 2009, T138, 014001

[7] Reimerders H. *et al*. 2020 *Nucl. Fusion* **60** 066030

[8] Senichenkov I. et al. 2021 *Plasma Phys. Control. Fusion* **63** 055011

[9] Kaveeva E. et al. 2021 Nucl. Mater. Energy **28** 101030

[10] Giroud C. et al. 2021 *Nucl. Fusion* in press

[11] Abe S. *et al.* 2019 *Nucl. Materials and Energy* **19** 390-396

[12] Park J.-S. *et al.* 2021 *Nucl. Fusion* **61** 016021

[13] Sytova E. et al. 2019 *Nucl. Mater. and Energy* **19** 72-78

[14] Rozhansky V. et al. 2018 *Contrib. Plasma Phys.* **58** 540

[15] Reimold F. et al. 2017 *Nucl. Mater. Energy* **12** 193

[16] Eich T.*et al.* 2020 *Nucl. Fusion* **60** 056016

[17] Rudakov D. *et al.* 2002 *Plasma Phys. Control. Fusion* **44** 717–731

[18] Eich T. et al. Nucl. Fusion **53** (2013) 093031

[19] Chang C.S. et al. 2017 *Nucl. Fusion* **57** 116023

[20] Li Z.-Y. *et al.* 2019 *Nucl. Fusion* **59** 046014

[21] Rozhansky V. 2014 *Contrib. Plasma Phys.* **54** 508 – 516

[22] Stangeby P. C. “The plasma boundary of magnetic fusion devices” 2000 IOP publishing Ltd.

[23] Goldston R. J. Nucl. Fusion **52** (2012) 013009

[24] Helander P. Sigmar D. “Collisional Transport in Magnetized Plasmas”, 2005 Cambridge University Press

[25] Senichenkov I. Yu. 2014 *Plasma Phys. Control. Fusion* **56** 055002

[26] Dux R. et al. 2020 *Nucl. Fusion* **60** 126039